OasisMap30: A 30m annual land cover dataset of China's oases from 1987 to 2024

Peng Chen[1], Qiang Tang[1], Yanxu Liu[2], Yuchuan Luo[1], Linhai Cheng[1], Yijia Wang[3], Wenxuan Xu[1], Shuai Wang[2]

[1]Chongqing Jinfo Mountain Karst Ecosystem National Observation and Research Station, School of Geographical Sciences, Southwest University, Chongqing, 400715, China
[2]State Key Laboratory of Earth Surface Processes and Hazards Risk Governance, Faculty of Geographical Science, Beijing Normal University, Beijing, 100875, China
[3]School of Geography, South China Normal University, Guangzhou, 510631, China

Correspondence to: Qiang Tang (qiangtang@swu.edu.cn)

Abstract. High spatio-temporal resolution maps of oasis land cover are valuable for understanding ecological and societal development processes in dryland regions. However, the relatively late development of oasis research, combined with the highly fragmented structure of oases and their frequent land cover transitions, has made it challenging to construct high spatio-temporal resolution land cover datasets for oases. As a result, dedicated data products of this kind are still lacking. Here, we developed a framework for annual 30 m land cover mapping that integrates Landsat satellite imagery, machine learning, a temporal segmentation approach (LandTrendr), and principal component analysis. Using this framework, we produced a 30 m resolution annual land-cover dataset for Chinese oases (OasisMap30) for the period 1987–2024 on the Google Earth Engine (GEE) platform. Accuracy assessment based on more than 6,300 visually interpreted samples demonstrates high accuracy of OasisMap30 (overall accuracy >90%). In cross-product comparisons based on visually interpreted and third-party test samples, OasisMap30 exhibits considerable advantages in terms of classification accuracy and error reduction. Moreover, in comparison with several 30 m resolution thematic products for impervious surface, cropland, and surface water, we found an impressive consistency between OasisMap30 and these datasets. Using OasisMap30, we investigated the changes in land cover patterns of Chinese oases. The results show that oasis area expanded by 45.87% (+7.75 Mha) between 1987 and 2024, primarily driven by cropland expansion and grassland restoration. Specifically, 4.04 Mha of desert were restored to grassland, and 3.19 Mha were converted from desert to cropland. In addition, OasisMap30 reveals the expansion of impervious surfaces (0.58 Mha) and surface water (0.35 Mha), as well as conversions among land cover types, such as the conversion of 3.12 Mha of grassland to cropland. Overall, the consistent, high-resolution OasisMap30 data can substantially support studies on the evolution of oasis landscape patterns, socio-ecological responses, and spatial pattern optimization, thereby contributing to the sustainable development of oasis regions. The full archive of OasisMap30 is freely available at https://doi.org/10.6084/m9.figshare.30798032 (Chen et al., 2025).

1 Introduction

Oases are the most productive and vulnerable landscapes in drylands (Chen et al., 2024a). An oasis is generally defined as an area with relatively flat terrain, sufficient water resources and high productivity, capable of supporting human activities such as agriculture, animal husbandry and industrial production, with deserts serving as the surrounding landscape matrix (Lin et al., 2024; Zhou et al., 2015). Over the past few decades, Chinese oases have undergone pronounced changes in their extent and internal structure under the combined influences of climate change and human activities (Zeng et al., 2019). In particular, the continued expansion of cropland and grassland has supported rapid increases in regional food and livestock production, but has also altered the relationships among water resources, food production and ecosystems in oasis regions (Chen et al., 2024b). These shifts have led to a range of ecological and hydrological problems, including groundwater decline, soil desiccation, vegetation degradation and intensified desertification, thereby sharpening the tension between oasis development and environmental sustainability (Chen et al., 2024a). Therefore, understanding how changes in oasis landscape patterns affect regional ecological and hydrological conditions is crucial for alleviating this tension (Lin et al., 2024). This knowledge also supports progress towards several sustainable development goals (SDGs), particularly SDG 15.3 on land degradation neutrality in drylands, as well as SDG 2 on food security and SDG 6 on sustainable water management (UN., 2015). However, due to the relatively late development of the oasis discipline, as well as difficulties in delineating oasis boundaries and highly fragmented internal land cover, high spatio-temporal resolution land-cover datasets for oasis regions are still lacking.

Remote sensing technology provides a vital means for monitoring land-cover information (Yang and Huang, 2021). With advancements in satellite and remote sensing technologies, the spatial and temporal resolution of mapping has significantly improved (Tu et al., 2024). The quality of land classification data directly affects the accuracy of studies related to land-cover changes. Because oases exhibit strong interannual variability, the precision of each map used for monitoring oasis dynamic is crucial (Xie et al., 2014). In annual change analyses, classification errors in individual maps can accumulate over time and introduce substantial uncertainties into the final results (Zhu, 2017). Reducing per-map errors is therefore particularly important.

To address this issue, previous studies have employed methods such as spatio-temporal filtering, consistency checks, and disturbance-based time-series analysis to improve the accuracy of land-cover products (Li et al., 2015; Zhu, 2017). Among these, the LandTrendr algorithm (Landsat-based detection of trends in disturbance and recovery) has shown excellent performance in detecting abrupt surface changes (Pasquarella et al., 2022). LandTrendr fits a piecewise linear trajectory to the full per-pixel time series of data values, effectively denoising interannual variability and smoothing long-term trends (Kennedy et al., 2010). From the fitted segments, it identifies disturbance events and quantifies their magnitude, timing and duration. These metrics can then be used to detect both abrupt surface-change events and longer-term change trends (Tu et al., 2024). However, when LandTrendr is applied to individual spectral bands or indices, a disturbance signal in a single variable (for example, near-infrared reflectance or the normalized difference vegetation index) may not be sufficient to confirm a true land-cover change. Robust land-cover change detection therefore requires integrating information from multiple indicators and

focusing on changes that are coherent across them. Principal component analysis (PCA) provides a way to reduce dimensionality by summarizing information from multiple correlated variables into a few composite components (Mugiraneza et al., 2020). By applying PCA to the disturbance magnitudes of multiple indicators derived from the LandTrendr algorithm, these disturbance signals can be integrated into a single composite metric. This integrated disturbance signal allows land-cover change areas to be identified more reliably than when relying on any individual index alone.

The aim of this study is to develop a new framework for annual land cover mapping at fine resolution, combining machine learning and a temporal segmentation algorithm. Based on this framework, we integrated multi-source remote sensing data and employed a combination of random forest, LandTrendr algorithm and principal component analysis to produce an annual 30 m resolution land cover dataset for Chinese oases (OasisMap30) from 1987 to 2024. In addition, this study also involved the following tasks: 1) assessing the accuracy of OasisMap30 using visually interpreted and third-party test samples; 2) validating the performance of OasisMap30 through inter-comparison with existing land-cover datasets and thematic datasets; and 3) investigating long-term land-cover changes in China's oases land cover over the past four decades.

2 Methodology

2.1 Delineation of China's oasis extent

To determine where oases are located across China, we first compiled oasis distributions reported in previous studies (Gao, 1987; Wei et al., 2018; Xie et al., 2014; Zhou et al., 2017). These literature-based maps were combined with NDVI information to obtain an initial, coarse delineation of potential oasis areas for the period 1987–2024. On this basis, we manually inspected the imagery and masked out mountain regions and clearly unvegetated deserts (e.g., the Taklamakan Desert), and then outlined the final study area to be classified on the GEE platform. To ensure that oases which may have disappeared by 2024 but existed in earlier years are not overlooked, land cover classification was performed over a region larger than the previously observed oasis extent. Within this study area, we classified land cover into seven types: impervious surface, surface water, cropland, shrubland, forest, grassland and barren land. According to the definition of oasis, all land-cover types other than barren land were considered oasis landscapes.

2.2 Data source

We used all available Landsat Level 2 Tier 1 surface reflectance (SR) data (TM 5, ETM+ 7, OLI 8) covering our study area from 1987 to 2024, with these data having undergone atmospheric correction. Considering the differences between Landsat sensors, we applied conversion factors recommended by Roy et al. (2016) to normalize Landsat 8 reflectance to Landsat 5 and 7 reflectance. This ensures comparability between multi-temporal images across years. Digital elevation data were sourced from the Shuttle Radar Topography Mission (SRTM).

2.3 Feature space construction

Based on Landsat imagery and SRTM DEM data, we collected and calculated metrics for random forest classification (Breiman,
95 2001). Among these, slope, aspect, and hillshade were computed from the DEM data. To enhance classification performance, we further applied the tasseled cap transformation to obtain brightness, greenness, and wetness indices using coefficients provided by Crist et al.(1985). The final feature indicators comprise four categories: spectral features, terrain feature, tasseled-cap transform, and gray-level co-occurrence matrix. The calculation methods for each indicator are detailed in Supplementary Table 1.

100 **Table1.** Independent variables of the random forest model for land-cover classification.

Feature indicators	Independent variables
Spectral feature	ρ_{Blue}, ρ_{Green}, ρ_{Red}, ρ_{Nir}, ρ_{SWI1}, ρ_{SWI2}, Normalized difference vegetation index (NDVI), Modified normalized difference water index (MNDWI), Normalized difference built-up index (NDBI)
Terrain feature	Elevation, Slope, Aspect, Hillshade
Tasseled-cap transform	Wetness index, Brightness index, Greenness index
Gray-level co-occurrence matrix	Entropy, Correlation, Variance, Contrast, Angular second moment, Inverse difference moment

Note: ρ_{Blue}, ρ_{Green}, ρ_{Red}, ρ_{Nir}, ρ_{SWI1}, ρ_{SWI2} are the surface reflectance values in the blue, green, red, near infrared, shortwave infrared 1, and 2 bands of the Landsat image, respectively.

2.4 Baseline 2024 oasis land-cover mapping

We used a random forest algorithm for land-cover classification (Figure 1). We first imported Landsat images into GEE and
105 performed pre-processing, including cloud and snow masking and mosaicking. Second, sample points from different land-cover types were selected from the pre-processed Landsat images. By combining these with Google Earth historical imagery, different land-cover types could be accurately and efficiently identified. Third, we used these sample points to construct a collection of image features that included spectral features, terrain features, tasseled cap transformation and gray-level co-occurrence matrix features (Table 1). These features were used to train a random forest classifier, with a ratio of 7:3 between
110 training and validation samples. The oasis land-cover map for 2024 produced by the random forest was then corrected by visual interpretation to obtain the final 2024 oasis land-cover dataset. To ensure its accuracy, six experts independently conducted visual inspection and manual corrections based on high-resolution imagery.
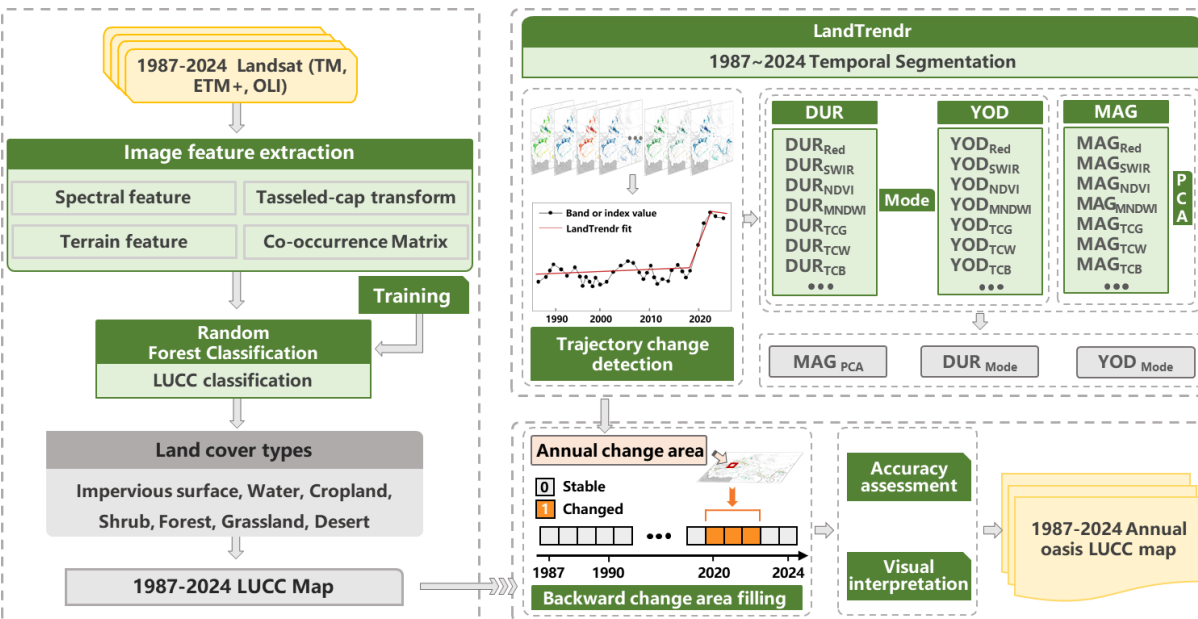
Figure 1: Flowchart of this study for mapping annual oasis land-cover. DUR: disturbance duration; YOD: year of disturbance; MAG: disturbance magnitude.

2.5 LandTrendr–PCA-based annual land-cover mapping

Land-cover classification is prone to error propagation, especially when producing annual map series, where classification errors can accumulate over time. Employing the LandTrendr algorithm to identify areas exhibiting abrupt changes in surface reflectance, followed by machine learning classification of these areas, can effectively reduce the impact of error propagation. To map land-cover dynamics from 1987 to 2024 while limiting the propagation of classification errors, we used the 2024 oasis land-cover dataset as a reference and applied the LandTrendr algorithm to the annual time series of spectral indices.

Since a single index's change cannot conclusively indicate land-cover change (for example, abrupt shifts in near-infrared reflectance or NDVI do not necessarily imply land-cover change), we combined LandTrendr with PCA to more accurately identify the locations and timing of land-cover change. For each pixel, we first extracted the disturbance magnitude (MAG), year of disturbance (YOD) and duration (DUR) from the fitted temporal trajectory for each index. We then applied PCA to the disturbance magnitudes of multiple indices to derive a single composite disturbance metric (MAGPCA), which integrates consistent disturbance signals across indices. Pixels exhibiting significant disturbance were flagged as candidate land-cover change areas. Subsequently, by taking the mode values of DUR and YOD distribution for all indicators, we obtained DURmode and YODmode maps, thereby defining the time windows for potential transitions.

Based on these candidate change areas and time windows, annual land-cover classification was performed for pixels identified as potentially changed, using the same feature types as for 2024 but with Landsat imagery from the corresponding years. Pixels without detected disturbance retained their land-cover class from the 2024 reference map or from the pre-disturbance period,

thereby limiting the temporal propagation of classification errors. Finally, the annual oasis land-cover maps for 1987–2024 were visually inspected and manually corrected by six experts, ensuring the consistency and reliability of the complete time series.

2.6 Evaluation of disturbance timing consistency

Because we used YOD_{mode} as the starting time for surface changes, dispersion in YOD across indices could interfere with the accurate identification of the true onset time of disturbance and thus affect classification accuracy. To verify the accuracy of the disturbance timing identified by this method, we examined the dispersion of the YOD distribution across indices (Eq. 1). The results indicate that $YOD_{indicator}$ exhibits a high degree of consistency. In addition, after identifying the years in which land cover may have changed, we have to further detect whether land cover types have changed through land cover classification and visual interpretation, and if not, this process will be repeated for the next year. Therefore, $YOD_{dispersion} > 0$ in this study has a limited impact on the identification of land cover change.

$$YOD_{dispersion} = YOD_{indicator} - YOD_{mode} \tag{1}$$

where $YOD_{indicator}$ indicates the YOD identified by the different indicators, and $YOD_{dispersion}$ indicates the dispersion of YOD. When the $YOD_{dispersion} = 0$, $YOD_{indicator}$ is consistent with YOD_{mode}; when $YOD\_dispersion < 0$, $YOD_{indicator}$ is earlier than YOD_{mode}; and when $YOD_{dispersion} > 0$, $YOD_{indicator}$ is later than YOD_{mode}.

2.7 Accuracy and error assessment

We used a visually interpreted test dataset (at least 6,300 samples annually) and a third-party test dataset (Geo-Wiki) to evaluate the accuracy of OasisMap30 (Fritz et al., 2017). To assure the spatial uniformity and spatial balance across land cover types in the validation of the visually interpreted test samples, we employed a stratified random sampling method based on a hexagonal grid. Specifically, the study area was divided into approximately 1,100 independent units using regular hexagons with a 10 km side length. Each unit was treated as an independent sampling unit for land cover type sampling, ensuring an even distribution of validation samples across the entire area. For each independent hexagon, the area proportion of seven land-cover types was calculated based on 30 m resolution land cover data. Stratified random sampling was then conducted according to these proportions and the predetermined total sample size. This method accounts for spatial distribution uniformity and land cover area proportions, effectively reducing sampling bias in validation samples. During the evaluation, five experts independently interpreted the data, and each validation point was confirmed by at least two researchers. For points with disagreements, a third researcher made the final decision. If interpretations remain controversial, the point is discarded. We ensured that the number of validation points for rare land cover classes (e.g., forest) was no fewer than 50, as recommended by Olofsson et al. (2014). After removing points with low confidence from each land cover class, we retained at least 6,300 validation samples annually.

Finally, we assessed the accuracy of OasisMap30 quantitatively using producer accuracy (PA), user accuracy (UA), overall accuracy (OA), and the F1 score. The F1 score represents the balance between producer accuracy and user accuracy (Eq. 2).

165 And we estimated the accuracy, area of each land-cover type, and uncertainty of the oasis map at 95% confidence intervals. For a detailed description of the estimation methods, see Olofsson et al.(2014).

$$F1 = 2\frac{PA \times UA}{(PA+UA)} \times 100\% \tag{2}$$

2.8 Datasets inter-comparison

We compared OasisMap30 with several widely applied and well-validated land cover products, including CLCD (Yang and
170 Huang, 2021), GLC_FCS30 (Zhang et al., 2021), ESACCI_LC (Defourny et al., 2017) and MCD12Q1 (Table S2). In addition, we assessed the accuracy of OasisMap30 through inter-comparison with 30 m resolution thematic data derived from Landsat imagery. The current primary impervious surface datasets covering oasis regions include Global Impervious Surface Area (GISA) (Huang et al., 2021) and Global Artificial Impervious Area (GAIA) (Gong et al., 2020). Crop-related thematic datasets mainly comprise Global Land Analysis & Discovery Cropland Data (GLAD) (Potapov et al., 2021), The Hybrid Cropland
175 Maps of China (CCropland30) (Zhang et al., 2024), and the Annual Cropland Dataset of China (CACD) (Tu et al., 2024). For surface water, the Global Surface Water (GSW) dataset was selected (Pekel et al., 2016). Compared with OasisMap30, GSW provides a much denser temporal record (monthly). To facilitate comparison, we calculated annual mean surface-water extent from the monthly GSW data. These thematic datasets have been shown to have good accuracy in previous studies.
To assess the spatial consistency between OasisMap30 and the thematic products, we first aggregated the 30 m datasets to a
180 $0.05° \times 0.05°$ spatial grid. For each grid cell, we then calculated the fractional area for each category and used these values to construct scatterplots. The coefficient of determination (R^2) and root mean square error (RMSE) were used to assess the level of consistency between OasisMap30 and the thematic products.

3 Result

3.1 The accuracy and error verification of the OasisMap30

185 Based on all available Landsat imagery data on GEE, we produced a 30 m resolution annual Chinese oasis land cover dataset. Verification results based on visually interpreted samples indicate that OasisMap30 has a high accuracy rate (Figure. 2). Overall accuracy ranges from 90.40% to 94.05%, with a mean of 91.96 ± 1.55% (Figure S1h). Among each category, cropland achieved the highest F1 score (93.25% ± 1.93%), followed by surface water (92.14% ± 2.09%), grassland (91.50% ± 1.06%), barren land (90.68% ± 0.47%), and impervious surfaces (87.49% ± 3.69%), while the average F1 scores for forest and
190 shrubland also exceed 84% (Figure S1). In addition, we evaluated the error and uncertainty of OasisMap30 using the methods recommended by Olofsson et al.(2014). Taking 2022 as an example, cropland and grassland areas in Chinese oases are estimated at 12.81 Mha and 8.48 Mha, with associated errors of only 0.133 Mha and 0.134 Mha, respectively (Table S3). Shrubland and forest have the largest classification errors among all land cover types, but their error ranges are still limited to 0.55 ± 0.05 Mha and 0.29 ± 0.034 Mha (Table S3). These evaluation results further demonstrate the robustness of OasisMap30.
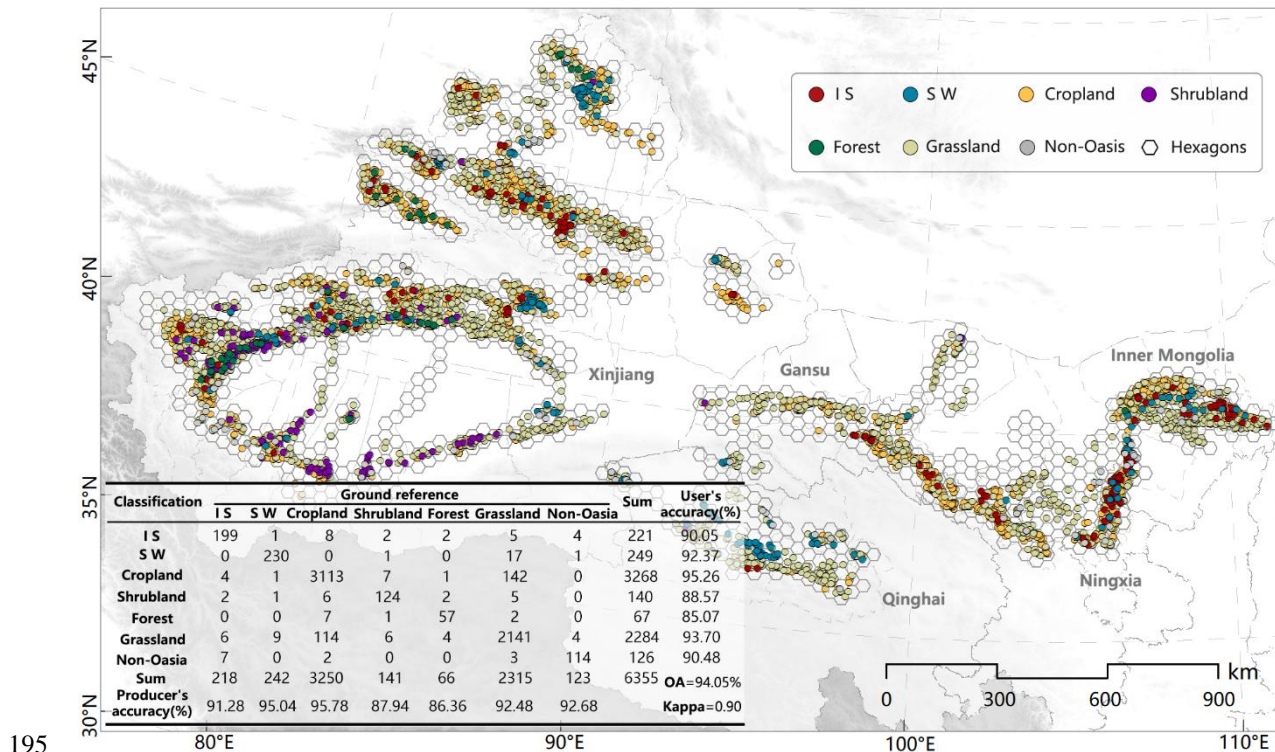
Figure 2: Accuracy assessment of the OasisMap30 dataset based on visually interpreted samples (taking the year 2024 as an example). I S: Impervious surface; S W: Surface water.

3.2 Comparison with existing Land cover datasets

Cross-dataset comparisons show that, for oasis regions in China, OasisMap30 exhibited substantially higher overall accuracy (93.64% in 2022) than CLCD (75.72%), GLC_FCS30 (74.13%), ESACCI_LC (66.22%) and MCD12Q1 (50.55%) (Table S4-24). For each land cover category, OasisMap30 achieved higher and more stable F1 scores compared to datasets such as CLCD, GLC_FCS30, and ESACCI_LC (Figure S1). OasisMap30 also showed a good ability to capture fine-scale details of oasis land cover (Figure. 3). We further evaluated the accuracy of OasisMap30 using Geo-Wiki test samples (Table S25). The results showed that OasisMap30 achieves an overall accuracy of 74.36%, substantially higher than that of the other datasets (50.09–60.90%). For individual land cover classes, OasisMap30 also showed consistently higher classification accuracy than the four comparison datasets.
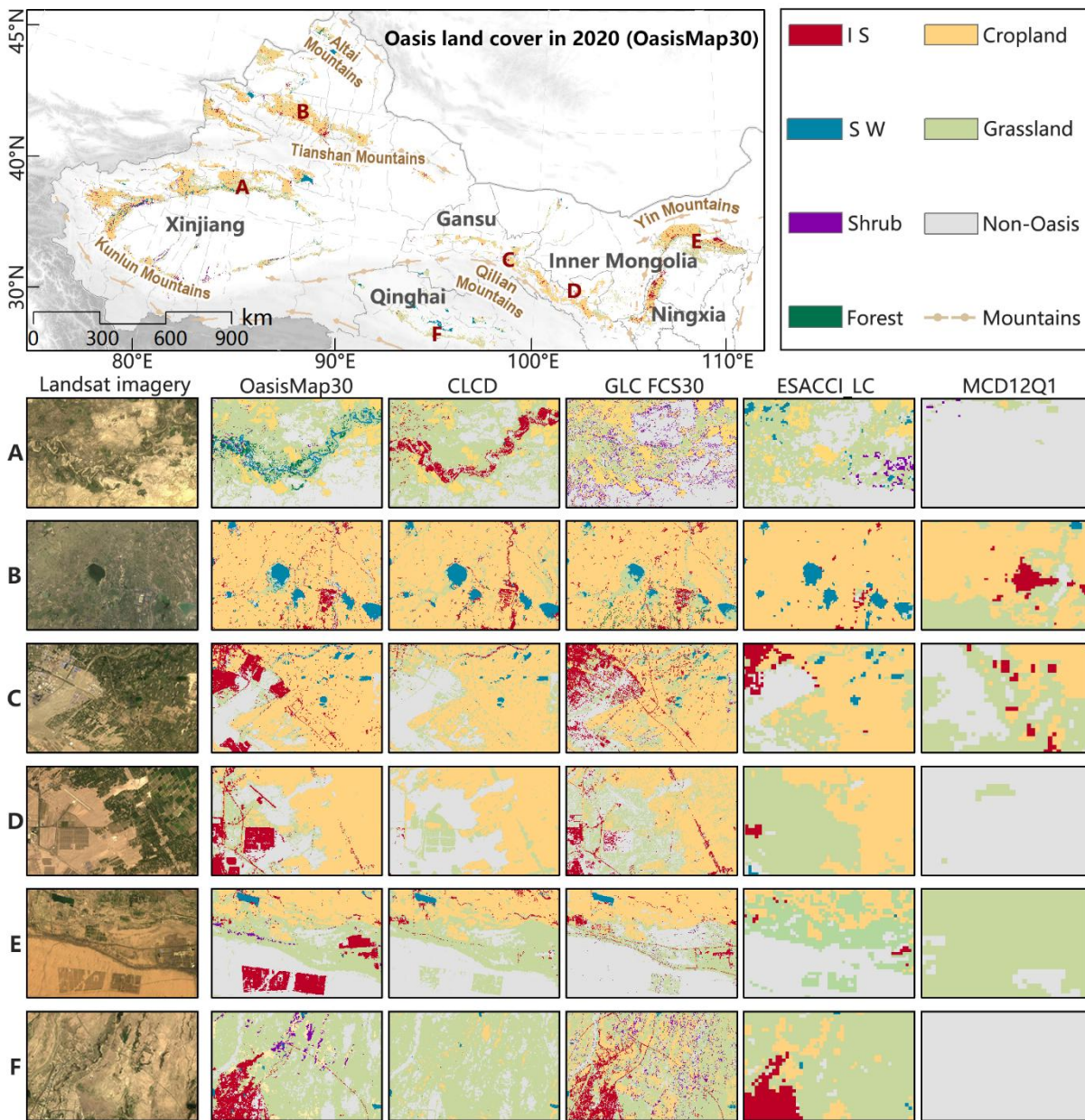
Figure 3: Regional comparison of oasis land-cover products. The first column shows Landsat imagery. Columns two to six display the spatial distribution of oasis land cover from OasisMap30 and four existing land-cover datasets. I S: Impervious surface; S W: Surface water. All the Landsat images are freely provided by USGS.

3.3 Comparison with other 30-m thematic products

Based on the GISA and GAIA datasets, we found that the impervious surface area within oasis regions exhibited a gradual expansion trend between 1987 and 2024, at rates of 0.014 Mha·yr⁻¹ and 0.037 Mha·yr⁻¹, respectively. The statistical results from OasisMap30 demonstrate good consistency with those from the two datasets (0.019 Mha·yr⁻¹). Moreover, the trends in

215 cropland and surface water changes estimated by OasisMap30 also exhibit well agreement with the results from thematic datasets. We did not conduct comparative analyses for grasslands due to the lack of a 30-m resolution grassland thematic dataset covering China's oasis regions. However, validation results based on visually interpreted samples and third-party test samples provide evidence that the grassland classification within OasisMap30 exhibits a high accuracy (Table S4-S9, S25).
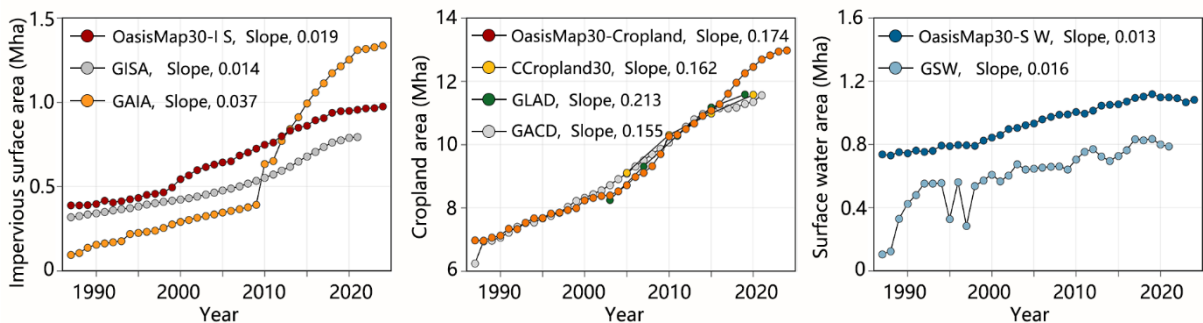
220 **Figure 4:** Comparison of temporal changes in different land cover areas of Chinese oases between OasisMap30 and various thematic datasets from 1987 to 2024. I S: Impervious surface; S W: Surface water.

3.3.1 Comparison with the spatial distribution of cropland thematic data

We assessed the accuracy of OasisMap30 in capturing the spatial dynamics of cropland through inter-comparison with GLAD, CCropland30, and CACD data. The scatter plot in Figure 5 shows the fraction of cropland after aggregating 30m data into

225 $0.05° \times 0.05°$ spatial grids. It was found that OasisMap30-cropland showed high consistency with CLAD, CCropland30, and CACD data in spatial distribution ($0.88 < R^2 < 0.93$), indicating that OasisMap30 has a high reliability in cropland classification.
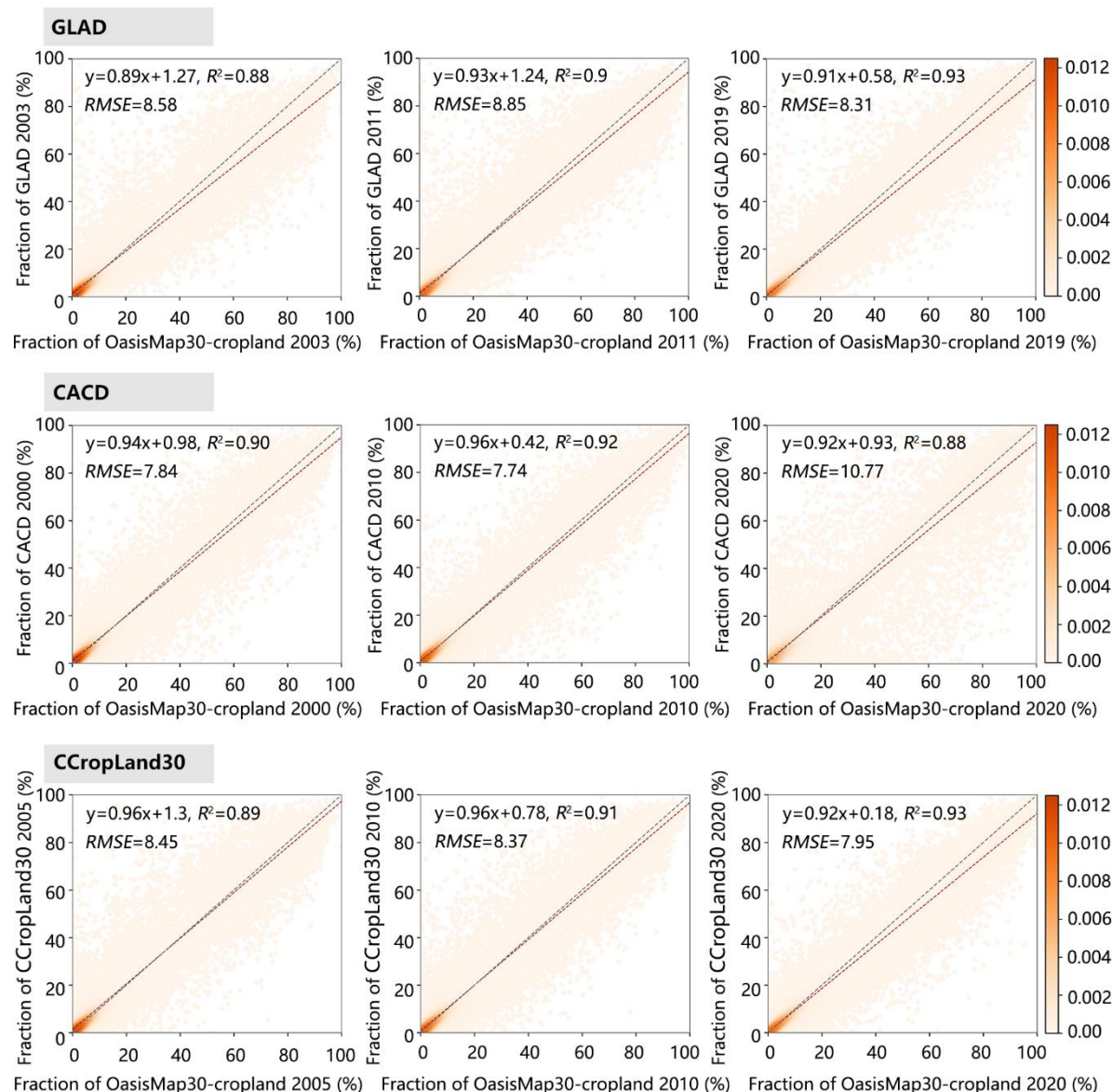
Figure 5: Scatter plots of cropland fraction between the OasisMap30, GLAD, CACD and CCropland30. Cropland fraction was aggregated within the 0.05°×0.05° spatial grid.

3.3.2 Comparison with the spatial distribution of surface water thematic data

Surface water trends in oasis regions over the past decades exhibit substantial spatial heterogeneity due to the comprehensive implications of human activities and climate change. We aggregated the surface water fraction of OasisMap30 and GSW data into 0.05°×0.05° spatial grids, and then assessed the accuracy of OasisMap30 in identifying oasis surface water dynamics (Figure 6). High decision coefficients ($0.8 < R^2 < 0.88$) indicate strong consistency between OasisMap30-Water and GSW data.

235
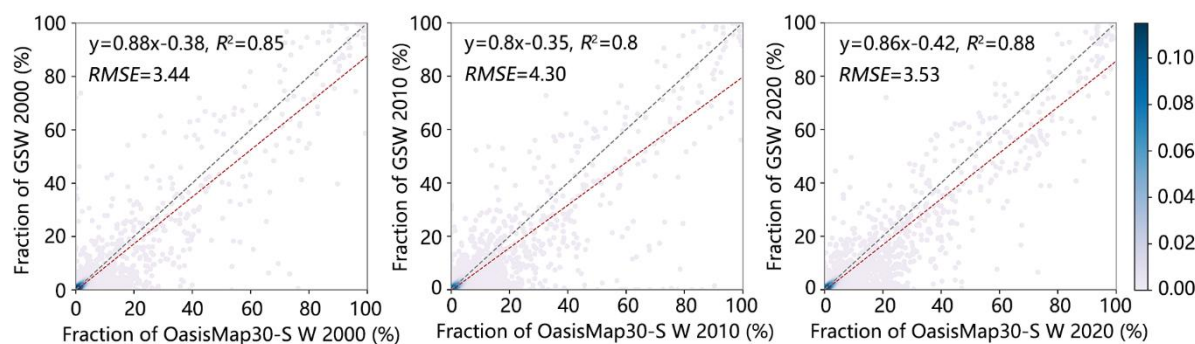
Figure 6: Scatterplots of surface water fraction between the OasisMap30 and GSW. Surface water fraction was aggregated within the 0.05°×0.05° spatial grid. S W: Surface water.

3.3.3 Comparison with the spatial distribution of impervious surface thematic data

The area of impervious surfaces serves as a key indicator for urbanization. With rapid economic development, the urbanization

240 level in China's oasis regions has gradually increased. We assessed the accuracy of impervious surface in OasisMap30 through inter-comparison o with impervious surface thematic datasets (Figure 7). By calculating the impervious surface fraction within 0.05°×0.05° spatial grids, we found high consistency between OasisMap30 with GAIA and GISA ($0.62 < R^2 < 0.85$). Moreover, the R^2 between OasisMap30-IS and two products exceeded 0.84 in 2020, indicating the reliability of OasisMap30.
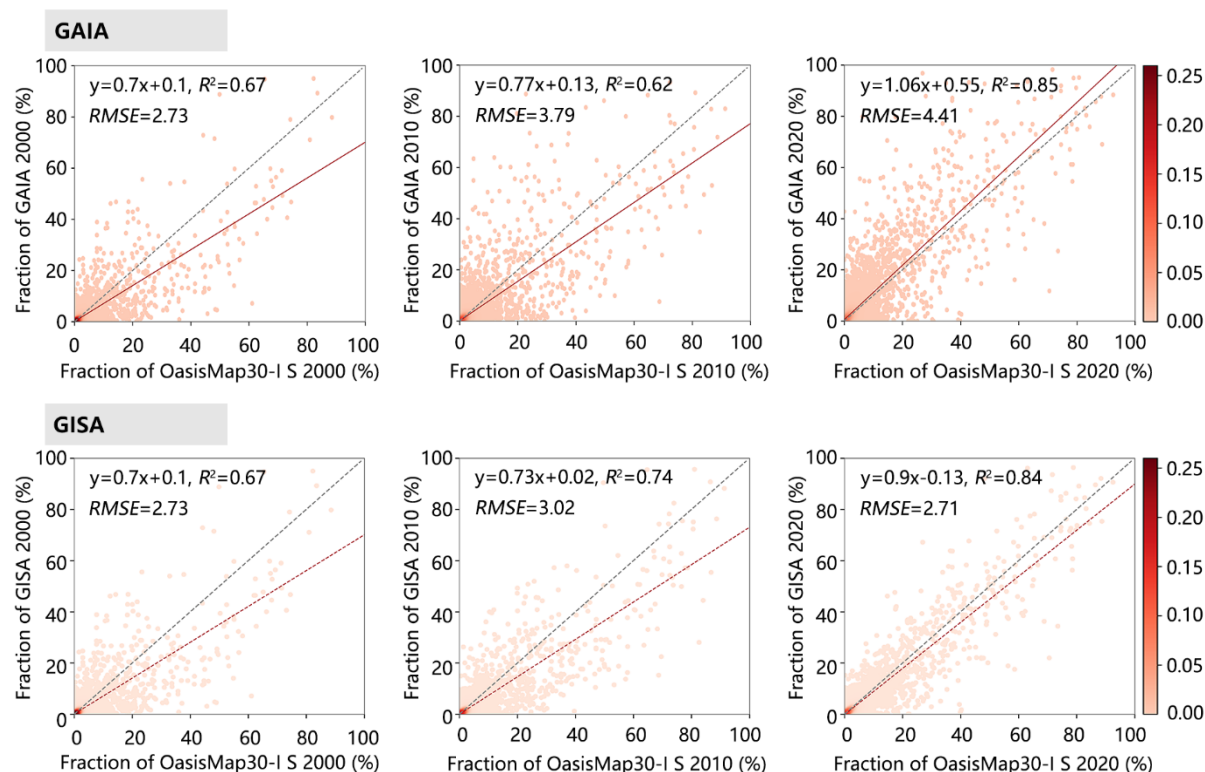
Figure 7: Scatterplots of impervious surface fraction between the OasisMap30, GAIA and GASA. Impervious surface fraction was aggregated within the 0.05°×0.05° spatial grid. IS: Impervious surface.

3.4 Dynamics of land cover in China's oases from 1987 to 2024

Over the past few decades, Chinese oases have undergone rapid expansion. Between 1987 and 2024, oasis area increased from 16.90 Mha to 24.65 Mha, at a rate of 0.22 Mha yr^{-1} (Figure 8a). Among land cover types, cropland exhibited the fastest expansion rate, followed by impervious surfaces. To compensate for the loss of large areas of high-quality cropland in southern China and to safeguard national food security under increasing population pressure, oases and the surrounding deserts, which are among important strategic reserve lands in China, have been extensively converted to cropland (Kuang et al., 2022). Statistics derived from OasisMap30 show that cropland area within oases expanded from 6.97 Mha to 12.98 Mha during this period, at a rate of 0.17 Mha yr^{-1}. Due to the high expansion rate, cropland gradually replaced grassland to become the largest land cover type within oases. The implementation of several livelihood-related policies has also accelerated the urbanization process in oasis areas (Figure S3), contributing to an expansion of impervious surfaces from 0.39 Mha to 0.97 Mha. Moreover, grassland areas increased from 8.21 Mha to 8.76 Mha at a rate of 0.008 Mha yr^{-1}, while forest and shrubland areas also showed slight growth, attributable to the implementation of ecological restoration projects (Figure S3). Benefiting from glacial melt due to climate warming, increased precipitation, and the construction of reservoirs and hydropower stations (Zhang et al., 2022; Huang et al., 2025), the area of surface water in oasis regions has continuously increased (+0.35 Mha). Notably, the trends in the areas of oases and each land type indicated by OasisMap30 are largely consistent with those of datasets such as CLCD and CFC_FCS30 (Figure 8).

Earth System
Science
Data

Open Access | Discussions
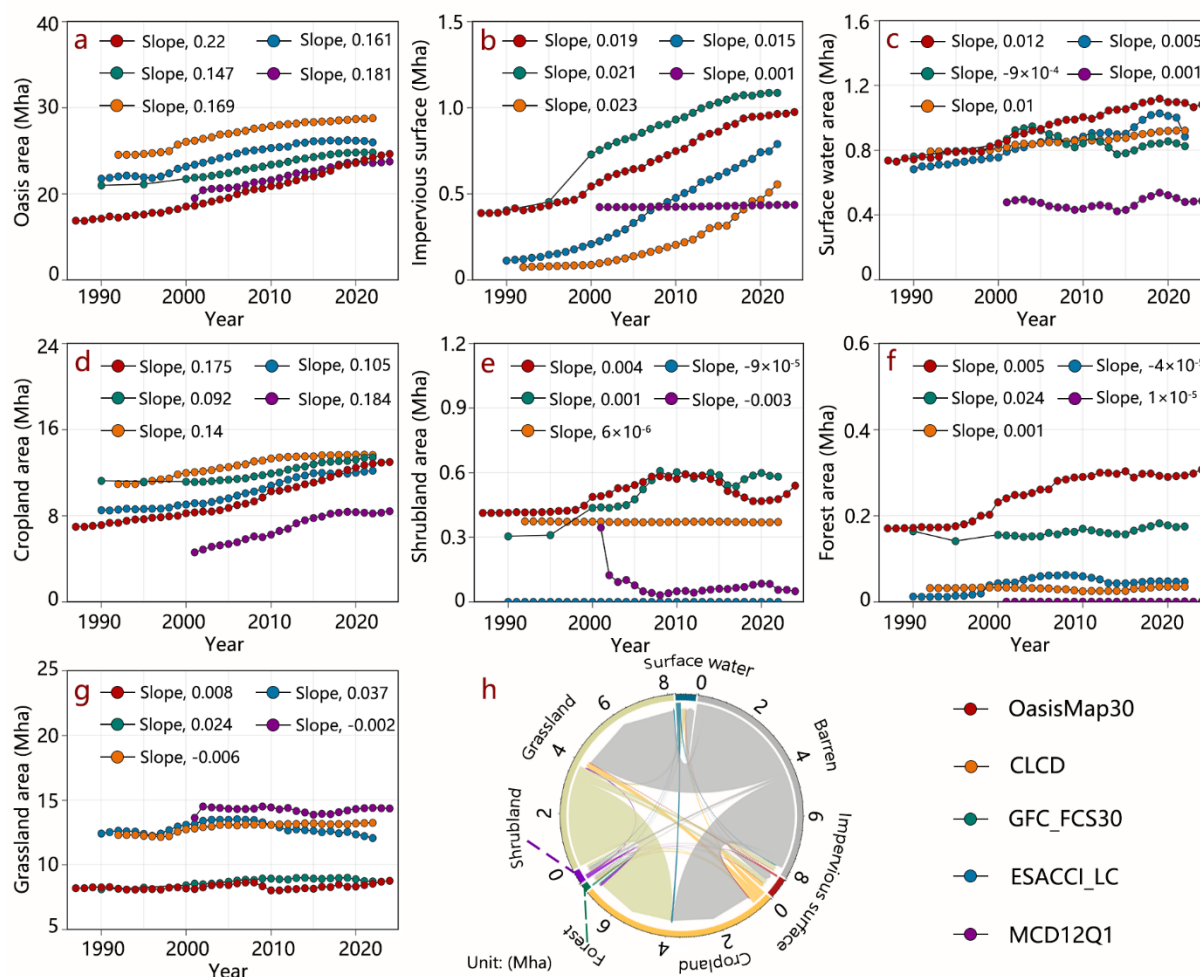
Figure 8: Comparison of temporal changes in different land cover areas of Chinese oases between OasisMap30 and various land cover
datasets from 1987 to 2024 (a-g); Changes of seven land cover types during the period of 1987-2024 in oasis of China.

At the provincial level, oases are unevenly distributed across five provinces. Xinjiang has the largest oasis area among the five
provinces, accounting for 66.24% of the total oasis area in China by 2024, followed by Inner Mongolia, Gansu, Qinghai, and
Ningxia (13.74%, 10.84%, 5.14%, and 4.04%, respectively) (Figure S2). Xinjiang not only ranks first among provinces in
terms of cropland expansion, but also shows the fastest increase in impervious surface area, driven by the rapid sprawl of cities
like Urumqi over recent decades (Wu et al., 2025). Qinghai exhibited the fastest expansion rate of surface water area. With the
warming and moistening climate, inflow runoff to the principal lakes of the Qaidam Basin has progressively increased,
resulting in a rapid expansion of surface water area at a rate of 0.006 Mha yr^{-1} in the Qinghai oasis region (Lu et al., 2025).
The Inner Mongolia Autonomous Region saw the largest net increase in grassland area (0.91 Mha), which can be primarily
attributed to the successful reversal of desertification in desert regions such as Kubuqi (Chen et al., 2022).

275   Based on the OasisMap30 dataset, we further revealed the process of land-cover conversion in oasis regions. Overall, grassland restoration contributed the most to the expansion of oasis areas, followed by the cropland reclamation (Figure 8h). Between 1987 and 2024, 4.04 Mha of barren land was successfully restored to grassland, accounting for 50.56% of the oasis's newly expanded area. Concurrently, 3.19 Mha of barren land was cultivated to cropland, accounting for 39.94% of the oasis expansion. With the expansion of cropland and grassland, many previously scattered and isolated oases in northwest China gradually

280   expanded and merged into a contiguous oasis belt, demonstrating a representative pattern of oasis evolution in China (Figure S4).

Within the oasis, land cover transitions are widely recorded. The largest land cover conversion pattern is grassland converted to cropland. During this period, 3.12 Mha of grassland within the oasis were converted to cropland, which resulted in cropland gradually surpassing grassland to become the dominant land cover type within oases. A total of 45.00% of the impervious

285   surface area gain came from barren land (such as the rapidly expanding photovoltaic panels in regions like Kubuqi and the Hexi Corridor) (Xia et al., 2024), while 52.21% came from the grassland and cropland (e.g., Ganzhou, Zhangye) (Zhou et al., 2015; Liu et al., 2019). The expansion of surface water primarily stems from grasslands (24.63%) and barrens (60.94%). This conversion is highly correlated with the warming and moistening trend in northwest China, where accelerated glacial melting and gradually increasing precipitation have provided more water resources to oasis regions (Yao et al., 2022). Ecological water

290   conveyance engineering (such as those for the Juyan Lake and Taitema Lake) also played a positive role in the expansion of surface water area (Wang et al., 2019; Ling et al., 2020). Overall, OasisMap30 performs excellently in capturing land cover changes, and can provide valuable support for studies on human-environment relationships, water-food-ecosystem nexus, and environmental sustainability in oasis regions.

3.5 Limitations and prospects

295   Due to differences between the Landsat 5 TM, 7 ETM+ and 8 OLI sensors, as well as the lack of high-quality remote sensing imagery in earlier years (Figure S5-S6), we were forced to use remote sensing images from adjacent years. This may have resulted in some land cover changes being overlooked. Spatially, there may be variations in mapping accuracy across different regions. Due to the extremely sparse vegetation in oasis-desert buffer zones, delineating oasis boundaries only with Landsat imagery can be challenging. Consequently, some sparsely vegetated buffer zones may be misclassified as barren. In the future,

300   the increased availability of field-based land cover survey data, combined with optical and high-resolution remote sensing imagery, will facilitate more precise delineation of oasis boundaries. Moreover, the dispersion of YOD between different indicators based on the LandTrendr algorithm may impact result accuracy. We have reduced the inevitable misclassification of land cover in mapping through visual interpretation, while complete error correction cannot be guaranteed. In the future, the integration of the USGS Landsat global archive will provide more historical Landsat imagery for the GEE platform. As

305   the availability of high-quality Landsat images increases, the accuracy of oasis mapping will be further improved.

4 Data availability

The OasisMap30 product generated in this study can be accessed at https://doi.org/10.6084/m9.figshare.30798032 (Chen et al., 2025). Landsat SR, SRTM, MCD12Q1, GLAD, and GSW(v1.2) were acquired from the Google Earth Engine (available at http://code.earthengine.google.com, last access: 9 December 2025). CLCD and GLC_FCS30 were provided by Wuhan University (available at https://doi.org/10.5281/zenodo.4417810, last access: 9 December 2025) and Aerospace Information Research Institute, Chinese Academy of Sciences (available at https://doi.org/10.5281/zenodo.3986872, last access: 9 December 2025). The ESACCI_LC was assessed from the European Space Agency climate office (available at https://doi.org/10.24381/cds.006f2c9a, last access: 9 December 2025). The GISA and GAIA were obtained from the Wuhan University (available at https://doi.org/10.5281/zenodo.5136330, last access: 9 December 2025) and Tsinghua University (available at https://doi.org/10.6084/m9.figshare.27245775, last access: 9 December 2025). The CACD and CCropland30 were provided by Tsinghua University (available at https://doi.org/10.5281/zenodo.7936885, last access: 9 December 2025) and National Tibetan Plateau Data Center (available at https://doi.org/10.11888/Terre.tpdc.301077, last access: 9 December 2025).

5 Conclusions

Oases represent the most productive yet also the most ecologically fragile regions in drylands, serving as the core areas for human production, livelihoods and economic development. Given the importance of oases, producing a high spatio-temporal resolution land cover datasets for oases are essential for revealing the patterns of oasis evolution and its impact on the ecological environment. This study developed a new framework for high spatio-temporal resolution land cover mapping and produced an annual 30 m resolution land-cover dataset for Chinese oases (namely OasisMap30). Accuracy assessments and comparisons with other datasets show that OasisMap30 performs well in terms of both reliability and capturing the dynamic changes in oases. Based on OasisMap30, we found that Chinese oases have undergone rapid expansion in recent decades. Between 1987 and 2024, oasis area increased from 16.89 Mha to 24.64 Mha at a rate of 0.22 Mha per year, with cropland expansion and grassland restoration being the main drivers of this gradual growth. In addition, we also observed large-scale land-cover conversions within oases, such as 3.12 Mha of grassland converted to cropland. The 30 m resolution OasisMap30 dataset is expected to provide important support for oasis landscape planning, water resource management, and research on socio-ecological interactions in drylands.

Author contributions

PC and SW designed the research, PC conducted the research and wrote the initial draft, PC and QT reviewed and edited the paper before submission. All authors participated in the review and discussion of the manuscript.

Competing interests

335 The contact author has declared that none of the authors has any competing interests.

Acknowledgements

The authors are grateful to all the data contributors who made it possible to complete this research.

Financial support

This work was supported by "the Fundamental Research Funds for the Central Universities" under Grant (SWU-KQ 25002).

340 **References**

Breiman, L.: Random Forests, Machine Learning, 45, 5–32, https://doi.org/10.1023/A:1010933404324, 2001.

Chen, P., Wang, S., Song, S., Wang, Y., Wang, Y., Gao, D., and Li, Z.: Ecological restoration intensifies evapotranspiration in the Kubuqi Desert, Ecological Engineering, 175, 106504, https://doi.org/10.1016/j.ecoleng.2021.106504, 2022.

Chen, P., Wang, S., Liu, Y., Wang, Y., Song, J., Tang, Q., Yao, Y., Wang, Y., Wu, X., Wei, F., and Feng, S.: Spatio-Temporal

345 Dynamics of Aboveground Biomass in China's Oasis Grasslands Between 1989 and 2021, Earth's Future, 12, e2023EF003944, https://doi.org/10.1029/2023EF003944, 2024a.

Chen, P., Tang, Q., Liu, Y., Luo, Y., Cheng, L., Xu, W., Wang, Y., and Wang, S.: OasisMap30: A 30m annual land cover dataset of China's oases from 1987 to 2024, https://doi.org/10.6084/m9.figshare.30798032.v1, 2025.

Chen, Y., Fang, G., Li, Z., Zhang, X., Gao, L., Elbeltagi, A., Shaer, H. E., Duan, W., Wassif, O. M. A., Li, Y., Luo, P., Selmi,

350 A., Yu, R., Yang, J., Hu, Y., Liu, C., Long, Y., Malik, I., Fu, A., Wistuba, M., Yang, Y., Zhu, C., and Gao, Y.: The Crisis in Oases: Research on Ecological Security and Sustainable Development in Arid Regions, Annual Review of Environment and Resources, 49, 1–20, https://doi.org/10.1146/annurev-environ-111522-105932, 2024b.

Crist, E. P.: A TM Tasseled Cap equivalent transformation for reflectance factor data, Remote Sensing of Environment, 17, 301–306, https://doi.org/10.1016/0034-4257(85)90102-6, 1985.

355 Defourny, P., Bontemps, S., Lamarche, C., Brockmann, C., Boettcher, M., Wevers, J., Kirches, G., and Santoro, M.: Land Cover CCI Product User Guide – Version 2.0, 2017.

Fritz, S., See, L., Perger, C., McCallum, I., Schill, C., Schepaschenko, D., Duerauer, M., Karner, M., Dresel, C., Laso-Bayas, J.-C., Lesiv, M., Moorthy, I., Salk, C. F., Danylo, O., Sturn, T., Albrecht, F., You, L., Kraxner, F., and Obersteiner, M.: A global dataset of crowdsourced land cover and land use reference data, Sci Data, 4, 170075,

360 https://doi.org/10.1038/sdata.2017.75, 2017.

Gao, H.: The distribution and types of oases in china (in china), Arid Land Geography, 10, 23–29, 1987.

Gong, P., Li, X., Wang, J., Bai, Y., Chen, B., Hu, T., Liu, X., Xu, B., Yang, J., Zhang, W., and Zhou, Y.: Annual maps of global artificial impervious area (GAIA) between 1985 and 2018, Remote Sensing of Environment, 236, 111510, https://doi.org/10.1016/j.rse.2019.111510, 2020.

Huang, E., Zhu, G., Meng, G., Wang, Y., Chen, L., Miao, Y., Wang, Q., Shi, X., Zhao, L., Wang, Q., Qi, X., Zhang, X., Jiao, Y., Lu, S., Li, R., and Li, W.: Historical dataset of reservoir construction in arid regions, Sci Data, 12, 1428, https://doi.org/10.1038/s41597-025-05712-3, 2025.

Huang, X., Li, J., Yang, J., Zhang, Z., Li, D., and Liu, X.: 30 m global impervious surface area dynamics and urban expansion pattern observed by Landsat satellites: From 1972 to 2019, Sci. China Earth Sci., 64, 1922–1933, https://doi.org/10.1007/s11430-020-9797-9, 2021.

Kennedy, R. E., Yang, Z., and Cohen, W. B.: Detecting trends in forest disturbance and recovery using yearly Landsat time series: 1. LandTrendr — Temporal segmentation algorithms, Remote Sensing of Environment, 114, 2897–2910, https://doi.org/10.1016/j.rse.2010.07.008, 2010.

Kuang, Liu, J., Tian, H., Shi, H., Dong, J., Song, C., Li, X., Du, G., Hou, Y., Lu, D., Chi, W., Pan, T., Zhang, S., Hamdi, R., Yin, Z., Yan, H., Yan, C., Wu, S., Li, R., Yang, J., Dou, Y., Wu, W., Liang, L., Xiang, B., and Yang, S.: Cropland redistribution to marginal lands undermines environmental sustainability, National Science Review, 9, nwab091, https://doi.org/10.1093/nsr/nwab091, 2022.

Li, X., Gong, P., and Liang, L.: A 30-year (1984–2013) record of annual urban dynamics of Beijing City derived from Landsat data, Remote Sensing of Environment, 166, 78–90, https://doi.org/10.1016/j.rse.2015.06.007, 2015.

Lin, J., Gui, D., Liu, Y., Liu, Q., Zhang, S., and Liu, C.: A high-precision oasis dataset for China from remote sensing images, Sci Data, 11, 726, https://doi.org/10.1038/s41597-024-03553-0, 2024.

Ling, H., Guo, B., Yan, J., Deng, X., Xu, H., and Zhang, G.: Enhancing the positive effects of ecological water conservancy engineering on desert riparian forest growth in an arid basin, Ecological Indicators, 118, 106797, https://doi.org/10.1016/j.ecolind.2020.106797, 2020.

Liu, Y., Song, W., and Deng, X.: Understanding the spatiotemporal variation of urban land expansion in oasis cities by integrating remote sensing and multi-dimensional DPSIR-based indicators, Ecological Indicators, 96, 23–37, https://doi.org/10.1016/j.ecolind.2018.01.029, 2019.

Lu, C., Zhang, Q., Woolway, R. I., Ma, L., Liu, T., Wang, G., Sun, D., Singh, V. P., Bai, Y., Sun, B., and Huang, X.: Global Warming Will Increase the Risk of Water Shortage in Northwest China, Earth's Future, 13, e2025EF006199, https://doi.org/10.1029/2025EF006199, 2025.

Mugiraneza, T., Nascetti, A., and Ban, Y.: Continuous Monitoring of Urban Land Cover Change Trajectories with Landsat Time Series and LandTrendr-Google Earth Engine Cloud Computing, Remote Sensing, 12, 2883, https://doi.org/10.3390/rs12182883, 2020.

Olofsson, P., Foody, G. M., Herold, M., Stehman, S. V., Woodcock, C. E., and Wulder, M. A.: Good practices for estimating area and assessing accuracy of land change, Remote Sensing of Environment, 148, 42–57, https://doi.org/10/f55gjk, 2014.

Pasquarella, V. J., Arévalo, P., Bratley, K. H., Bullock, E. L., Gorelick, N., Yang, Z., and Kennedy, R. E.: Demystifying LandTrendr and CCDC temporal segmentation, International Journal of Applied Earth Observation and Geoinformation, 110, 102806, https://doi.org/10.1016/j.jag.2022.102806, 2022.

Pekel, J.-F., Cottam, A., Gorelick, N., and Belward, A. S.: High-resolution mapping of global surface water and its long-term 400 changes, Nature, 540, 418–422, https://doi.org/10.1038/nature20584, 2016.

Potapov, P., Turubanova, S., Hansen, M. C., Tyukavina, A., Zalles, V., Khan, A., Song, X.-P., Pickens, A., Shen, Q., and Cortez, J.: Global maps of cropland extent and change show accelerated cropland expansion in the twenty-first century, Nat Food, 1–10, https://doi.org/10.1038/s43016-021-00429-z, 2021.

Roy, D. P., Kovalskyy, V., Zhang, H. K., Vermote, E. F., Yan, L., Kumar, S. S., and Egorov, A.: Characterization of Landsat-405 7 to Landsat-8 reflective wavelength and normalized difference vegetation index continuity, Remote Sensing of Environment, 185, 57–70, https://doi.org/10.1016/j.rse.2015.12.024, 2016.

Tu, Y., Wu, S., Chen, B., Weng, Q., Bai, Y., Yang, J., Yu, L., and Xu, B.: A 30 m annual cropland dataset of China from 1986 to 2021, Earth System Science Data, 16, 2297–2316, https://doi.org/10.5194/essd-16-2297-2024, 2024.

UN.: Transforming our world: The 2030 agenda for sustainable development, United Nations, New York, 35 pp., 2015.

410 Wang, S., Fu, B., Bodin, Ö., Liu, J., Zhang, M., and Li, X.: Alignment of social and ecological structures increased the ability of river management, Science Bulletin, 64, 1318–1324, https://doi.org/10.1016/j.scib.2019.07.016, 2019.

Wei, H., Xu, Z., Liu, H., Ren, J., Fan, W., Lu, N., and Dong, X.: Evaluation on dynamic change and interrelations of ecosystem services in a typical mountain-oasis-desert region, Ecological Indicators, 93, 917–929, https://doi.org/10/gjgnmc, 2018.

Wu, J., Wang, H., Wang, C., Huang, X., Wang, Z., Zhang, C., Chen, B., Yiming, Y., and Zhou, C.: Which exerts a greater 415 impact on ecosystem resilience: Cropland expansion or urban expansion? Insights from a spatiotemporal analysis, Ecological Informatics, 90, 103314, https://doi.org/10.1016/j.ecoinf.2025.103314, 2025.

Xia, Z., Li, Y., Guo, S., Chen, R., Zhang, W., Guo, X., Zhang, X., and Du, P.: Satellites Reveal Spatial Heterogeneity in Dryland Photovoltaic Plants' Effects on Vegetation Dynamics, Earth's Future, 12, e2024EF004427, https://doi.org/10.1029/2024EF004427, 2024.

420 Xie, Y., Gong, J., Sun, P., and Gou, X.: Oasis dynamics change and its influence on landscape pattern on Jinta oasis in arid China from 1963a to 2010a: Integration of multi-source satellite images, International Journal of Applied Earth Observation and Geoinformation, 33, 181–191, https://doi.org/10/gkbndk, 2014.

Yang, J. and Huang, X.: The 30 m annual land cover dataset and its dynamics in China from 1990 to 2019, Earth Syst. Sci. Data, 13, 3907–3925, https://doi.org/10.5194/essd-13-3907-2021, 2021.

425 Yao, J., Chen, Y., Guan, X., Zhao, Y., Chen, J., and Mao, W.: Recent climate and hydrological changes in a mountain–basin system in Xinjiang, China, Earth-Science Reviews, 226, 103957, https://doi.org/10.1016/j.earscirev.2022.103957, 2022.

Zeng, H., Wu, B., Zhu, W., and Zhang, N.: A trade-off method between environment restoration and human water consumption: A case study in Ebinur Lake, Journal of Cleaner Production, 217, 732–741, https://doi.org/10.1016/j.jclepro.2018.12.284, 2019.

Zhang, J., Wang, S., He, Y., Ren, Y., and Huang, J.: Contribution of the Precipitation-Recycling Process to the Wetting Trend
430 in Xinjiang, China, Journal of Geophysical Research: Atmospheres, 127, e2021JD036407, https://doi.org/10.1029/2021JD036407, 2022.

Zhang, L., Wang, W., Ma, Q., Hu, Y., Ma, H., and Zhao, Y.: CCropLand30: High-resolution hybrid cropland maps of China created through the synergy of state-of-the-art remote sensing products and the latest national land survey, Computers and Electronics in Agriculture, 218, 108672, https://doi.org/10.1016/j.compag.2024.108672, 2024.

435 Zhang, X., Liu, L., Chen, X., Gao, Y., Xie, S., and Mi, J.: GLC_FCS30: global land-cover product with fine classification system at 30m using time-series Landsat imagery, Earth System Science Data, 13, 2753–2776, https://doi.org/10.5194/essd-13-2753-2021, 2021.

Zhou, D., Wang, X., and Shi, M.: Human Driving Forces of Oasis Expansion in Northwestern China During the Last Decade—A Case Study of the Heihe River Basin, Land Degradation & Development, 28, 412–420, https://doi.org/10/f9r33m, 2017.

440 Zhou, S., Huang, Y., Yu, B., and Wang, G.: Effects of human activities on the eco-environment in the middle Heihe River Basin based on an extended environmental Kuznets curve model, Ecological Engineering, 76, 14–26, https://doi.org/10.1016/j.ecoleng.2014.04.020, 2015.

Zhu, Z.: Change detection using landsat time series: A review of frequencies, preprocessing, algorithms, and applications, ISPRS Journal of Photogrammetry and Remote Sensing, 130, 370–384, https://doi.org/10.1016/j.isprsjprs.2017.06.013, 2017.